Meson masses in large N_f QCD from the Bethe-Salpeter equation

Masayasu Harada,* Masafumi Kurachi,[†] and Koichi Yamawaki[‡]

Department of Physics, Nagoya University, Nagoya 464-8602, Japan
(Received 2 May 2003; published 1 October 2003)

We solve the homogeneous Bethe-Salpeter (HBS) equation for the scalar, pseudoscalar, vector, and axial-vector bound states of quarks and antiquarks in large N_f QCD with the improved ladder approximation in the Landau gauge. The quark mass function in the HBS equation is obtained from the Schwinger-Dyson (SD) equation in the same approximation for consistency with the chiral symmetry. Amazingly, because of the fact that the two-loop running coupling of large N_f QCD is explicitly written in terms of an analytic function, large N_f QCD turns out to be the first example in which the SD equation can be solved in the complex plane and hence the HBS equation directly in the time-like region. We find that approaching the chiral phase transition point from the broken phase, the scalar, vector, and axial-vector meson masses vanish to zero with the same scaling behavior, all degenerate with the massless pseudoscalar meson. This may suggest a new type of manifestation of the chiral symmetry restoration in large N_f QCD.

I. INTRODUCTION

Spontaneous chiral symmetry breaking is one of the most important properties to understand the low-energy phenomena of QCD in the real world. This chiral symmetry is expected to be restored in QCD at several extreme conditions such as QCD with a large number of massless quarks ("large N_f QCD", see, e.g., Refs. [1–7]), and QCD in hot and/or dense matter (see, e.g., Ref. [8]). In Ref. [2], based on the infrared (IR) fixed point existing at a two-loop beta function for a large number of massless quarks ($N_f \lesssim \frac{11}{2} N_c$) [1], it was found through the improved ladder Schwinger-Dyson (SD) equation that chiral symmetry restoration takes place for N_f such that $N_f^{\text{crit}} < N_f < \frac{11}{2} N_c$, where $N_f^{\text{crit}} \simeq 4 N_c (=12$ for $N_c =3)$. Then, in Ref. [3] this chiral restoration at N_f^{crit} was further identified with "conformal phase transition" which was characterized by the essential singularity scaling. Moreover, such chiral restoration is also observed by other various methods such as lattice simulation [5], dispersion relation [6], instanton calculus [7], effective field theoretical approach [9], etc.

More attention has been paid to the property of the phase transition. Especially, it is interesting to ask what are the light degrees of freedom near the phase transition point in the large N_f QCD: For example, in the manifestation of the chiral symmetry restoration *á la* the linear sigma model, the scalar bound state becomes a chiral partner of the pseudoscalar bound state and becomes massless at the phase transition point. On the contrary, in the vector manifestation (VM) [10,11] obtained by the effective field theoretical approach based on the hidden local symmetry model [12], it is the vector bound state which becomes massless as a chiral partner of the pseudoscalar bound state. Besides, from the viewpoint of the conformal phase transition [3], it is natural to

suppose that all the existing bound states become massless near the phase transition point when approached from the broken phase (see Ref. [13]).

Then, it is quite interesting to study which types of the bound states actually exist near the phase transition point, and investigate the critical behavior of their masses directly from QCD. Such studies from the first principle will give us a clue to understand the nature of the chiral phase transition in large N_f QCD.

A powerful tool to study the bound states of quark and antiquark directly from QCD is the homogeneous Bethe-Salpeter (HBS) equation in the (improved) ladder approximation (see, for reviews, Refs. [14–16]). When the mass of the quark is regarded as a constant, we can easily solve the HBS equation by using a so-called fictitious eigenvalue method [14]. However, for consistency with the chiral symmetry, the quark propagator in the HBS equation must be obtained by solving the SD equation with the same kernel as that used in the HBS equation [17–20], and as a result, the quark mass becomes a certain momentum dependent function. Then, in order to obtain the masses and the wave functions of the bound states, it is necessary to solve the HBS equation and the SD equation simultaneously.

When we try to solve these two equations in real-life ($N_f=3$) QCD, however, we encounter difficulties. First of all, for the consistency of the solution of the SD equation with QCD in a high energy region, we need to use the running coupling which obeys the evolution determined from QCD β-function in the high energy region (see, for reviews, Refs. [15,16]). Since the running coupling diverges at some infrared scale, Λ_{QCD}, we have to regularize the running coupling in the low energy region, for which there exist several ways (see, e.g., Refs. [21–25]). Even if we fix the infrared regularization in such a way that we can solve the SD equation on the real (space-like) axis, another problem arises when we try to solve the HBS equation. Since the argument of the quark mass function in the HBS equations for the massive bound states becomes a complex quantity after the Wick rotation has been made, we have to solve the SD equation on the complex plane, which requires an analytic con-

―――――――
*Electronic address: harada@eken.phys.nagoya-u.ac.jp
[†]Electronic address: kurachi@eken.phys.nagoya-u.ac.jp
[‡]Electronic address: yamawaki@eken.phys.nagoya-u.ac.jp

tinuation of the running coupling. Several works such as in Refs. [26,27] proposed models of running couplings for a general complex variable which are consistent with perturbative QCD for large space-like momentum. However, they still have branch cuts on the complex plane, and it is a complicated task to obtain the solution of the SD equation for a general complex variable. One way to avoid such a complication is solving the inhomogeneous BS equation for vertex functions to obtain the current correlators in the space-like region which we can fit the mass of the relevant bound state to (see, e.g., Refs. [28,29]). Another way might be replacing the entire running coupling with an *ad hoc* analytic function (see, e.g., Ref. [30]). Anyway, it is impossible to solve the SD equation on the complex plane without modeling the running coupling.

In this paper, we point out that the situation dramatically changes when we increase the number of massless quarks. When N_f becomes larger than $N_f^* \simeq 8.05$, the running coupling obtained from the renormalization group equation (RGE) with two-loop approximation takes a finite value for all the range of the energy region due to the emergence of the infrared (IR) fixed point. Then, we need no IR regularization, and we do not have any ambiguities coming from the regularization scheme which do exist in the case of small N_f. Moreover, an explicit solution of the two-loop RGE can be written in terms of the Lambert W function [4,31], and when N_f is close to $N_f^{\rm crit}$ the solution of the RGE has no singularity on the complex plane except for the time-like axis [31]. Consequently, we can solve the SD equation on the complex plane without introducing any models for the running coupling.

Based on these facts, we solve the HBS equations for the bound states of quark and antiquark in large N_f QCD with the improved ladder approximation in the Landau gauge. The mass function for complex arguments needed in the HBS equation is obtained by solving the SD equation with the same kernel as that used in the HBS equation. We find the solution of the HBS equation in each of the scalar, vector, and axial-vector channels, which implies that the scalar, vector, and axial-vector bound states are actually formed near the phase transition point. Our results show that the masses of the scalar, vector, and axial-vector bound states go to zero as the number of quarks N_f approaches to its critical value $N_f^{\rm crit}$ where the chiral symmetry restoration takes place. This may suggest the existence of a new type of manifestation of chiral symmetry restoration in large N_f QCD other than the linear sigma model-like manifestation and a simple version of the vector manifestation proposed in Ref. [10].

This paper is organized as follows. In Sec. II we numerically solve the SD equation with an approximate form of the running coupling, and study the critical behavior of the Nambu-Goldstone boson decay constant. In Sec. III we solve the SD equation for complex arguments. Section IV is devoted to summarizing the numerical method for solving the HBS equation. Section V is the main part of this paper. We first solve the HBS equation for the pseudoscalar bound state to show that the approximation adopted in the present analysis is consistent with the chiral symmetry. We next solve the HBS equation for the scalar, vector, and axial-vector bound
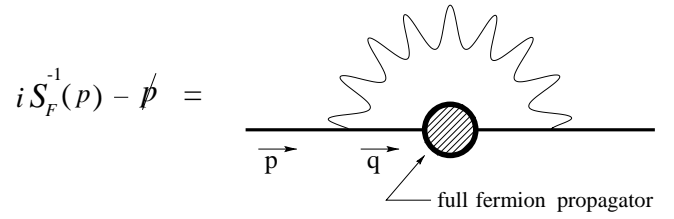

FIG. 1. A graphical expression of the SD equation in the (improved) ladder approximation.

states to obtain their masses. Finally we give a summary and discussion in Sec. VI. In Appendix A we solve the HBS equation for the orthopositronium with a constant electron mass to show the validity of the fictitious eigenvalue method. Bispinor bases for the bound states are listed in Appendix B. In Appendix C we calculate the coupling constants F_V, F_A, and G_S of the vector, axial-vector, and scalar bound states to the vector current, axial-vector current, and scalar density. We briefly study numerical uncertainties in the present analysis in Appendix D.

II. SCHWINGER-DYSON EQUATION IN LARGE N_f QCD

In this section we numerically solve the Schwinger-Dyson (SD) equation for the quark propagator with the improved ladder approximation in the Landau gauge, and show the critical behaviors of the dynamical mass and the decay constant of the Nambu-Goldstone boson. We also show the behavior of the fermion-antifermion pair condensate $\langle \bar{\psi}\psi \rangle$ near the phase transition point.

A. SD equation in the (improved) ladder approximation

The Schwinger-Dyson (SD) equation is a powerful tool to study the dynamical generation of the fermion mass directly from QCD (for reviews, see, e.g., Refs. [15,16]). The SD equation for the full fermion propagator $iS_F^{-1} = A(p^2)\not{p} - B(p^2)$ in the improved ladder approximation [22,21] is given by (see Fig. 1 for a graphical expression)

$$iS_F^{-1}(p) - \not{p} = C_2 \int \frac{d^4q}{i(2\pi)^4} \bar{g}^2(p,q)\frac{1}{(p-q)^2}$$

$$\times \left(g_{\mu\nu} - \frac{(p-q)_\mu(p-q)_\nu}{(p-q)^2} \right) \gamma^\mu iS_F(q)\gamma^\nu,$$

$$(2.1)$$

where $C_2[=(N_c^2-1)/2N_c]$ is the second casimir invariant, and $\bar{g}(p,q)$ is the running coupling. The Landau gauge is adopted for the gauge boson propagator.

The SD equation provides coupled equations for two functions A and B in the full fermion propagator S_F. When we use a simple ansatz for the running coupling, $\bar{g}^2(p,q) = \bar{g}^2(x), x \equiv \max(p_E^2, q_E^2)$ [22,21], with (p_E^2, q_E^2) being the Euclidean momenta, we can carry out the angular integration and get $A(p^2) \equiv 1$ in the Landau gauge. Then the SD equation becomes a self-consistent equation for the mass function
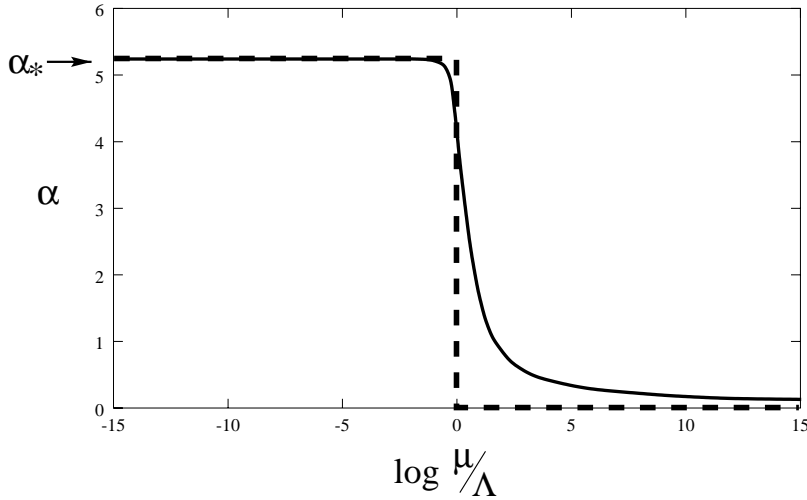
FIG. 2. Two-loop running coupling (solid line) compared with the approximate form in Eq. (2.9) (dashed line) for $N_f = 9$.

$\Sigma(p^2) \equiv B(p^2)$. The resultant asymptotic behavior of the dynamical mass $\Sigma(p^2)$ is shown to coincide with that obtained by the operator product expansion technique [15,16].

However, it was shown in Ref. [18] that the axial Ward-Takahashi identity is violated in the improved ladder approximation unless the gluon momentum is used as the argument of the running coupling as $\bar{g}^2[(p_E - q_E)^2]$. In this choice we cannot carry out the angle integration analytically since the running coupling depends on the angle factor $\cos\theta = p_E \cdot q_E / |p_E||q_E|$. Furthermore, we would need to introduce a nonlocal gauge fixing [18] to preserve the condition $A = 1$.

In Ref. [24], however, it was shown that an angle averaged from $\bar{g}^2(p_E^2 + q_E^2)$ gives a good approximation. Then, in the present analysis we take the argument of the running coupling as

$$\bar{g}^2(p_E, q_E) \Rightarrow \bar{g}^2(p_E^2 + q_E^2). \tag{2.2}$$

After applying this angle approximation and carrying out the angular integration, we can show (see, e.g., Refs. [32,33,15,16]) that A always satisfies $A(p^2) = 1$ in the Landau gauge. Then the SD equation becomes

$$\Sigma(x) = C_2 \frac{3}{16\pi^2} \int dy \, \frac{y\Sigma(y)}{y + \Sigma^2(y)} \frac{\bar{g}^2(x+y)}{\max(x,y)}, \tag{2.3}$$

where $x = p_E^2$ and $y = q_E^2$. Although the choice of arguments in Eq. (2.2) explicitly breaks the chiral symmetry as mentioned above, it will be shown later that the magnitude of the breaking is negligible.

B. Running coupling in large N_f QCD

In QCD with N_f flavors of massless quarks, the renormalization group equation (RGE) for the running coupling $\alpha(\mu)$ $[= \bar{g}^2(\mu)/4\pi]$ in the two-loop approximation is given by

$$\mu \frac{d}{d\mu} \alpha(\mu) = -b\alpha^2(\mu) - c\alpha^3(\mu), \tag{2.4}$$

where

$$b = \frac{1}{6\pi}(11N_c - 2N_f),$$

$$c = \frac{1}{24\pi^2}\left(34N_c^2 - 10N_cN_f - 3\frac{N_c^2 - 1}{N_c}N_f\right). \tag{2.5}$$

From the above beta function we can easily see that, when $b > 0$ and $c < 0$, i.e., N_f takes a value in the range of $N_f^* < N_f < \frac{11}{2}N_c$ ($N_f^* \simeq 8.05$ for $N_c = 3$), the theory is asymptotically free and the beta function has a zero, corresponding to an IR stable fixed point [1,2], at

$$\alpha_* = -\frac{b}{c}. \tag{2.6}$$

Existence of the IR fixed point implies that the running coupling takes a finite value even in the low energy region. Actually, the solution of the two loop RGE in Eq. (2.4) can be explicitly written [31,34] in all the energy region as

$$\alpha(\mu) = \alpha_*[W(\mu^{b\alpha_*}/e\Lambda^{b\alpha_*}) + 1]^{-1}, \tag{2.7}$$

where $W(x) = F^{-1}(x)$ with $F(x) = xe^x$ is the Lambert W function, and Λ is a renormalization group invariant scale defined by [2]

$$\Lambda \equiv \mu \exp\left[-\frac{1}{b\alpha_*}\log\left(\frac{\alpha_* - \alpha(\mu)}{\alpha(\mu)}\right) - \frac{1}{b\alpha(\mu)}\right]. \tag{2.8}$$

We note that, in the present analysis, we fix the value of Λ to compare the theories with a different number of flavors, and that we have no adjustable parameters in the running coupling in Eq. (2.7), accordingly (see discussion below). We show an example of $\alpha(\mu)$ for $N_f = 9$ by the solid line in Fig. 2.

The fact that the running coupling is expressed by a certain function as in Eq. (2.7) implies that, in the case of large N_f QCD, *we do not need to introduce any IR regularizations* such as the ones adopted in Refs. [21–23] for studying real-

life QCD with small N_f in which the IR regularization parameter must be chosen in such a way that the running coupling in the infrared region becomes larger than the critical value $\alpha_{cr} = \pi/4$ for realizing the dynamical chiral symmetry breaking [21]. The running coupling in large N_f QCD takes a certain value in the IR region for given N_f, so that we can definitely determine, within the framework of the SD equation, whether or not the dynamical chiral symmetry breaking is realized. Actually, the value of α_* decreases monotonically with increasing N_f, and the chiral symmetry restores when N_f becomes large enough. In Refs. [2,4], it was shown that the phase transition occurs at $N_f^{crit} \simeq 11.9$ for $N_c = 3$ (corresponding to $\alpha_* = \alpha_{cr} = \pi/4$).

In order to reduce the task of numerical calculations in solving the HBS equation, we modify the shape of the running coupling. Since the dynamics in the infrared region governs the chiral symmetry breaking, we adopt the following approximation for the running coupling [3,4]:

$$\frac{\bar{g}^2(x+y)}{4\pi} = \alpha_* \theta[\Lambda^2 - (x+y)].\qquad(2.9)$$

In this approximation the coupling takes the constant value α_* (the value at the IR fixed point) below the scale Λ and entirely vanishes in the energy region above this scale. The dashed line in Fig. 2 represents the approximated form of the running coupling for $N_f = 9$.

C. Numerical solution for the SD equation

In this section we briefly explain how we solve the SD equation numerically.

We first introduce the infrared (IR) cutoff λ_{SD} and ultraviolet (UV) cutoff Λ_{SD} as

$$\Lambda^2 e^{\lambda_{SD}/\Lambda} \leq x, \quad y \leq \Lambda^2 e^{\Lambda_{SD}/\Lambda}.\qquad(2.10)$$

Then, we discretize the momentum variable x and y into N_{SD} points as

$$x_i = \Lambda^2 \exp[\lambda_{SD}/\Lambda + D_{SD} \cdot i], \quad (i = 0,1,2,\ldots,(N_{SD}-1)),\qquad(2.11)$$

where

$$D_{SD} = \frac{(\Lambda_{SD} - \lambda_{SD})/\Lambda}{N_{SD} - 1}.\qquad(2.12)$$

Accordingly, the integration over y is replaced with a summation as

$$\int dy \Rightarrow D_{SD} \sum_j y_j.\qquad(2.13)$$

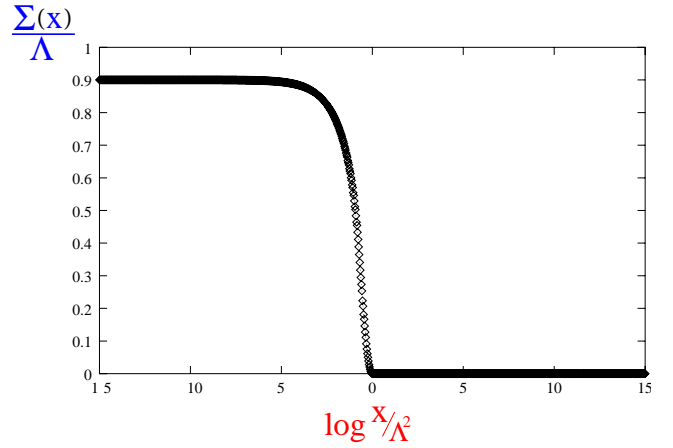Then, the SD equation in Eq. (2.3) with the running coupling in Eq. (2.9) is rewritten as

$$\text{FIG. 3. A solution of the discretized SD equation in Eq. (2.14) for } N_f = 9.$$

$$\Sigma(x_i) = \frac{1}{4\pi^2} D_{SD} \sum_j \bar{g}^2(x_i + y_j) \frac{y_j^2}{\max(x_i, y_j)} \frac{\Sigma(y_j)}{y_j + \Sigma^2(y_j)}.\qquad(2.14)$$

This discretized version of the SD equation is solved by the recursion relation:

$$\Sigma_{(n+1)}(x_i) = \frac{1}{4\pi^2} D_{SD} \sum_j \bar{g}^2(x_i + y_j)$$
$$\times \frac{y_j^2}{\max(x_i, y_j)} \frac{\Sigma_{(n)}(y_j)}{y_j + \Sigma_{(n)}^2(y_j)}.\qquad(2.15)$$

Starting from a suitable initial condition [we choose $\Sigma_{(0)}(x_i) = 1$], we update the mass function by the above recursion relation. Then, we stop the iteration when the convergence condition

$$D_{SD} \sum_i \frac{x_i^2}{16\pi^2} [\Sigma_{(n+1)}(x_i) - \Sigma_{(n)}(x_i)]^2 < \varepsilon^2 \Lambda^6\qquad(2.16)$$

is satisfied for sufficiently small ε, and regard this $\Sigma_{(n)}$ as a solution of Eq. (2.14). In Fig. 3, we show the numerical solution for the mass function $\Sigma(x)$.

Here, we took $N_f = 9$ ($\alpha_* \simeq 5.2$) as an example and used the following parameters:

$$\Lambda_{SD}/\Lambda = +15, \quad \lambda_{SD}/\Lambda = -15, \quad N_{SD} = 1000, \quad \varepsilon = 10^{-15}.\qquad(2.17)$$

Now, let us study the critical behavior of the fermion mass as N_f is varied. Note that we can use α_* instead of N_f as an input parameter, because once we choose a value of N_f, the value of α_* is uniquely determined from Eq. (2.6). For example, $\alpha_* = 1$ implies $N_f = 11.42$ and $\alpha_* = \alpha_{cr}$ implies $N_f = 11.91$. We solve Eq. (2.14) for various values of α_* and plot the values of $\Sigma(m^2)$ in Fig. 4.
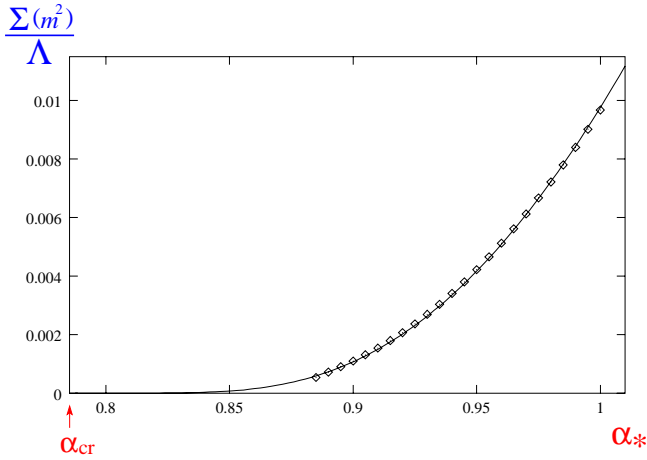
FIG. 4. Numerical solutions of $\Sigma(x=m^2)$ for several values of α_* (indicated by $\diamond$). The solid line shows the function in Eq. (2.19) with the best fitted value $d=4.0$.

Here, m represents the dynamical mass defined by $m=\Sigma(m^2)$. It should be noticed that m is defined in the space-like region which does not represent the pole mass of fermion. As we will show in Sec. III, the present fermion propagator does not have any poles and then there are no pole masses of fermion.

We compare this result with the analytic solution [3,4]:

$$\Sigma(m^2) \approx \Lambda \exp\left(-\frac{\pi}{\sqrt{\dfrac{\alpha_*}{\alpha_{cr}}-1}}\right) \quad \text{for } \alpha_* > \alpha_{cr}.$$

(2.18)

In the above form there is an ambiguity in the prefactor. Then, we introduce the function

$$h(\alpha_*) = d\Lambda \exp\left(-\frac{\pi}{\sqrt{\dfrac{\alpha_*}{\alpha_{cr}}-1}}\right),$$

(2.19)

and fit the value of the prefactor d by minimizing

$$\sum_{\alpha_*} |\Sigma(x=m^2;\alpha_*) - h(\alpha_*)|^2,$$

(2.20)

in the range of $\alpha_* \in [0.885:1]$. The resultant best fitted value of d is

$$d \simeq 4.0.$$

(2.21)

We plot the function in Eq. (2.19) with the best fitted value $d=4.0$ in Fig. 4 (solid line). This clearly shows that the α_* dependence of the resultant $\Sigma(m^2)$ from our numerical calculation is consistent with the analytic result: The dynamical mass function vanishes when α_* reaches the critical value $\alpha_{cr} = \pi/4$. Noting that decreasing α_* corresponds to increas-

ing N_f for fixed N_c as we discussed in the previous section, we see that the chiral symmetry restoration actually occurs at $N_f = N_f^{crit} \simeq 12(N_c/3)$ [2,4].

D. Pseudoscalar meson decay constant in large N_f QCD

So far we have solved the SD equation and obtained the mass functions for the various values of α_*. Now we can calculate the pseudoscalar meson decay constant F_P at each α_* by using the Pagels-Stokar formula [35]:

$$F_P^2 = \frac{N_c}{4\pi^2} \int dx \, \frac{x\Sigma^2(x) - \dfrac{x^2}{4}\dfrac{d}{dx}[\Sigma^2(x)]}{[x+\Sigma^2(x)]^2}.$$

(2.22)

In Fig. 5, we plot the values of F_P for several values of α_* (indicated by $\diamond$). To study the critical behavior of the pseudoscalar meson decay constant we use the function of the form in Eq. (2.19) and fit the value of d by minimizing

$$\sum_{\alpha_*} |F_P(\alpha_*) - h(\alpha_*)|^2,$$

(2.23)

for $\alpha_* \in [0.885:1]$. The resultant best fitted value of d is

$$d \simeq 1.5 (\equiv d_{F_P}).$$

(2.24)

We plot the fitting function with $d=1.5$ in Fig. 5 (dotted line). This shows that the results of the numerical calculations for F_P are well fitted by the function of the form in Eq. (2.19), and that the pseudoscalar meson decay constant has the same critical behavior as the mass function has.

E. Fermion-antifermion pair condensate

In this section, we calculate the fermion-antifermion pair condensate $\langle \bar{\psi}\psi \rangle$ in large N_f QCD, and show that the system
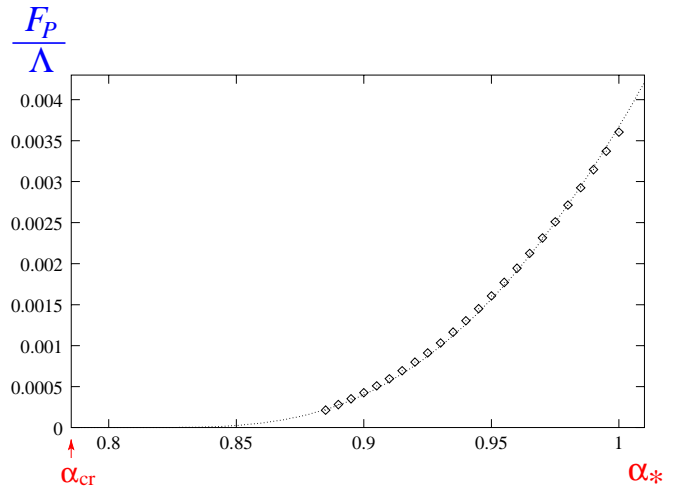

FIG. 5. Values of F_P calculated from the Pagels-Stokar formula for several values of α_* (indicated by $\diamond$). The dotted line shows the function of the form in Eq. (2.19) with the best fitted value $d = 1.5$.

in the present analysis has the large anomalous dimension γ_m for the operator $\bar{\psi}\psi$. We also show that the values of γ_m are not affected so much by the approximation for the running coupling used in the present analysis.

The condensate $\langle \bar{\psi}\psi \rangle$ is calculated from the following equation:

$$\langle \bar{\psi}\psi \rangle_{\Lambda_{\mathrm{UV}}} = -\frac{N_c}{4\pi^2} \int_0^{\Lambda_{\mathrm{UV}}^2} dx \, \frac{x\Sigma(x)}{x+\Sigma^2(x)}, \qquad (2.25)$$

where $\Sigma(x)$ is the mass function obtained from the SD equation and Λ_{UV} represents UV cutoff introduced to regularize the UV divergence. In the improved ladder approximation, the high-energy behavior of the mass function is consistent with that derived using the operator product expansion (OPE). The chiral condensate calculated using the mass function was shown to obey the renormalization group equation derived with the OPE (see, e.g., Refs. [15,16]). Then, as was adopted in Refs. [2–4], we identify the condensate, which is calculated with UV cutoff Λ_{UV}, with that renormalized at the scale Λ_{UV} in QCD.[1]

We expect that infrared dynamics in large N_f QCD is similar to that of strong coupling QED or walking gauge theories [36] since the running coupling in large N_f QCD is well approximated by the constant coupling (see Fig. 2) [4]. Then, we also expect that the value of the anomalous dimension in large N_f QCD becomes $\gamma_m \simeq 1$ since the walking gauge theories have $\gamma_m \simeq 1$ [36].

When a considering system has the anomalous dimension γ_m, scaling properties of F_P and $-\langle \bar{\psi}\psi \rangle$ with respect to α_* near the critical point are expressed as follows [36]:

$$F_P \sim m, \qquad (2.26)$$

$$-\langle \bar{\psi}\psi \rangle \sim m^{3-\gamma_m}, \qquad (2.27)$$

where m represents the dynamical fermion mass. These equations mean that the relation between $\langle \bar{\psi}\psi \rangle$ and F_P can be written as

$$-\langle \bar{\psi}\psi \rangle = c \cdot F_P^{3-\gamma_m}, \qquad (2.28)$$

where c is a certain positive constant. From this equation, we can express the anomalous dimension as

$$\gamma_m = \gamma_m' - \varepsilon, \qquad (2.29)$$

where

$$\gamma_m' = 3 - \frac{\log(-\langle \bar{\psi}\psi \rangle)}{\log F_P}, \qquad (2.30)$$

---

[1] When the condensate is calculated using the approximated running coupling defined by Eq. (2.9), the integration in Eq. (2.25) is effectively cut off at the scale of Λ due to the truncation of the running coupling for any values of $\Lambda_{\mathrm{UV}} > \Lambda$. [See Fig. 3: $\Sigma(x) = 0$ for $x > \Lambda^2$.]
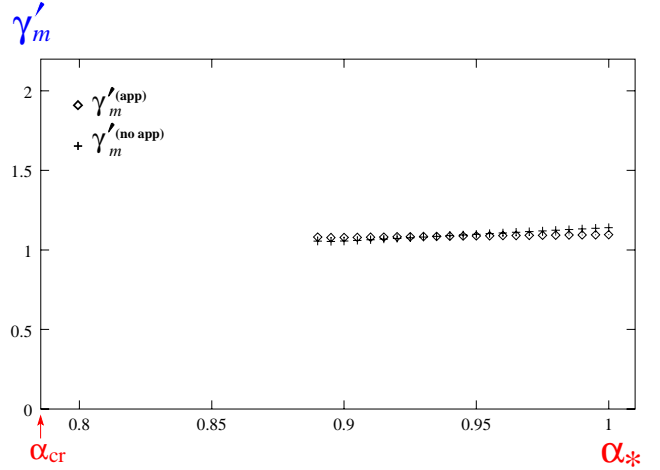

FIG. 6. Values of γ_m' for several values of α_*. $\diamond$ and $+$ represent the values of γ_m' calculated from Eq. (2.30) with and without approximation for the running coupling. (We call them $\gamma_m'^{(\mathrm{app})}$ and $\gamma_m'^{(\mathrm{no\text{-}app})}$ respectively.)

$$\varepsilon = \frac{\log c}{-\log F_P}. \qquad (2.31)$$

Here, we note that γ_m' approaches γ_m for $\alpha_* \to \alpha_{\mathrm{cr}}$ since F_P becomes small, i.e., $(-\log F_P) \gg 1$, near the critical point (see Fig. 5):

$$\varepsilon \to 0 \quad \text{for} \quad \alpha_* \to \alpha_{\mathrm{cr}}. \qquad (2.32)$$

In Fig. 6, we plot the values of γ_m' for several values of α_* as an estimation of the anomalous dimension.

The data indicated by $\diamond$ in Fig. 6 is obtained with the approximated running coupling (dashed line in Fig. 2) in the SD equation. (We call this kind of data $\gamma_m'^{(\mathrm{app})}$.) On the other hand, the data indicated by $+$ is the result from the calculation with the two-loop running coupling given in Eq. (2.7). (We call this kind of data $\gamma_m^{(\mathrm{no\text{-}app})}$.)[2] From these results, we

---

[2] The reason why we introduced the approximated running coupling (2.9) in the present analysis is to reduce the task of numerical calculations in solving the HBS equations. As for the SD equation, we can easily solve it numerically with the two-loop running coupling given in Eq. (2.7). Since we have to compare $\gamma_m'^{(\mathrm{app})}$ and $\gamma_m'^{(\mathrm{no\text{-}app})}$ at the same energy scale, we have lowered the scale of $\langle \bar{\psi}\psi \rangle^{(\mathrm{no\text{-}app})}$ from Λ_{UV} to Λ by the following two-loop renormalization group equation:

$$\langle \bar{\psi}\psi \rangle_\Lambda = \langle \bar{\psi}\psi \rangle_{\Lambda_{\mathrm{UV}}} \left[\frac{\alpha(\Lambda_{\mathrm{UV}})}{\alpha(\Lambda)} \right]^{\gamma_m^{(0)}/4\pi b}$$

$$\times \left[1 + \left(\frac{\gamma_m^{(1)}}{4\pi b} - \frac{2\gamma_m^{(0)}}{b^2} \right) \frac{\alpha(\Lambda) - \alpha(\Lambda_{\mathrm{UV}})}{4\pi} \right],$$

where,

$$\gamma_m^{(0)} = 6C_2, \qquad \gamma_m^{(1)} = C_2 \left(3C_2 + \frac{97}{3}N_c - \frac{10}{3}N_f \right).$$

conclude that large N_f QCD with two-loop running coupling as well as with approximated running coupling actually possesses[3]

$$\gamma_m \simeq \gamma'_m \simeq 1. \tag{2.33}$$

Moreover, Fig. 6 shows that the data of $\gamma'^{(app)}_m$ is in good agreement with that of $\gamma'^{(no-app)}_m$, which implies that the approximation for the running coupling used in the present analysis works well. We also expect that the approximation does not affect the results so much when we calculate the HBS equations for the bound states.

III. SD EQUATION ON THE COMPLEX PLANE

As we will discuss in Sec. IV, we need the mass function for complex arguments when we solve the HBS equation for the massive bound state. In this section, we first introduce the SD equation for the complex argument following Ref. [37] (see also Ref. [38]), and then solve it in the case of large N_f QCD.

The SD equation for the complex argument is expressed as [37]

$$\Sigma(x) = C_2 \frac{3}{16\pi^2} \left[\int_{C(0,x)} dy \frac{y}{x} + \int_{C(x,\infty)} dy \right] \frac{\bar{g}^2(x+y)\Sigma(y)}{y + \Sigma^2(y)}, \tag{3.1}$$

where $C(a,b)$ is the integral path on the complex plane. Here, we took the same argument of the running coupling as that in Eq. (2.2), and carried out the angle integration. Note that the integral path $C(a,b)$ must be taken so as to avoid the branch cut appearing in the integral.

We first study the structure of the running coupling appearing in the SD equation (3.1) to clarify the branch cut. In the improved ladder approximation it is essential to use the running coupling determined from the β-function in the high energy (space-like) region for consistency with perturbative QCD. In QCD with small N_f, however, the running coupling obtained from the perturbative β-function diverges at some infrared scale, Λ_{QCD}. In the ordinary SD equation in the space-like region, the infrared singularity is avoided by introducing infrared regularization such as the so-called Higashijima-Miransky approximation [21,22] and its extension as in Ref. [23]. However, since the running coupling in Eq. (3.1) is a complex function which has the complex argument, we need an extension with analyticity satisfied. Several works such as in Refs. [26,27] proposed models of running coupling which are consistent with perturbative QCD in the high energy region. But they still have branch cuts on the complex plane, and it is a burdensome task to evade all the branch cuts by carefully selecting the integral path in Eq. (3.1). One way to avoid such a complication might be to give

---

[3]From the values of c obtained by fitting to the data of $\langle \bar{\psi}\psi \rangle$, we find $\varepsilon = 0.04$–0.06 for the approximated running coupling, and $\varepsilon = 0.16$–0.25 for the two-loop running coupling.
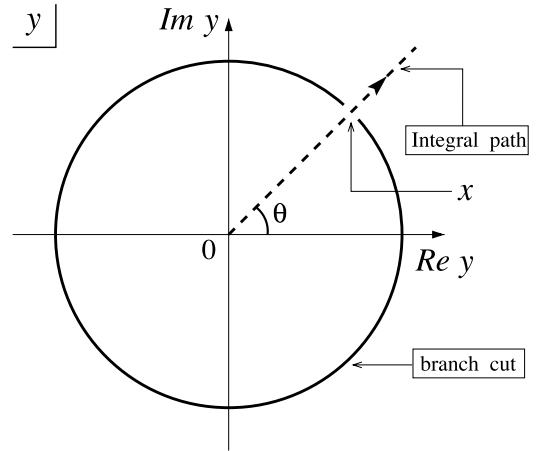

FIG. 7. Integral path of the SD equation (3.1). Here, the branch cut appears from the four-dimensional angle integration.

up the consistency with perturbative QCD and use models of running coupling with analyticity such as the one used in Ref. [30].

Here we point out that the situation dramatically changes in the large N_f QCD. In the case of large N_f QCD, as we explained in Sec. II B, the running coupling, as well as the two-loop β-function, is finite for any space-like momentum. This implies that we may be able to construct the running coupling by analytic continuation using the β-function. Actually, an explicit solution of the two-loop renormalization group equation (RGE) can be written in terms of the Lambert W function [4,31]. When N_f is close to N_f^{crit}, the solution of the RGE has no singularity on the complex plane except for the time-like axis [31].

As a result, for general complex x except on the time-like axis ($x < 0$), we can take the integral path $C(a,b)$ in such a way that it just avoids the branch cut coming from the angle integration. In Fig. 7 we show the branch cut together with a simple choice of the integral path [37].

We stress again that the reason why we can take this simple integral path is that the running coupling has no singularity on the complex plane except for the time-like axis.

For solving the SD equation on the complex plane, we here study the explicit form of the running coupling. In Fig. 8 we show the real part of the running coupling on the complex plane which is obtained by performing the analytic continuation from the running coupling on the real axis determined from the two-loop β-function.

This figure shows that Re $\alpha \simeq \alpha_*$, i.e., Im $\alpha \simeq 0$, in the range of $Y = |y| < \Lambda^2$, and that Re $\alpha \ll \alpha_*$ in the range of $Y > \Lambda^2$. Thus we take the following approximation for the running coupling on the complex plane:

$$\alpha(y) = \alpha_* \theta(\Lambda^2 - Y), \tag{3.2}$$

which is smoothly connected to the approximation adopted in Eq. (2.9) for the running coupling on the space-like axis.

Now, let us solve the SD equation (3.1) to obtain the mass function for complex variable x. Along the integral path shown in Fig. 7, the variables x and y are parametrized as
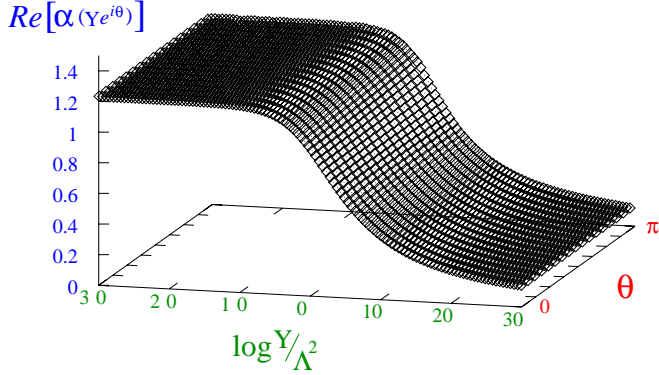
FIG. 8. Real part of the two-loop running coupling for $N_f = 11$ on the complex plane obtained by the analytic continuation from the running coupling on the real axis (we use the Cauchy-Rieman relation). The complex argument of α is expressed as $y = Ye^{i\theta}$, where Y and θ are real. Note that y is in the space-like region for $\theta = 0$ and in the time-like region for $\theta = \pi$.

$$x = Xe^{i\theta}, \quad y = Ye^{i\theta}, \tag{3.3}$$

where X, Y, and θ are real. Then the SD equation (3.1) is rewritten as

$$\Sigma(Xe^{i\theta}) = C_2 \frac{3}{16\pi^2} \left[\int_0^X dY \frac{Y}{X} + \int_X^\infty dY \right] \frac{\bar{g}^2(X+Y)\Sigma(Ye^{i\theta})}{Y + e^{-i\theta}\Sigma^2(Ye^{i\theta})}. \tag{3.4}$$

From this we can easily see that the solution is expressed as

$$\Sigma(x) = e^{i(\theta/2)}\bar{\Sigma}(X), \tag{3.5}$$

where $\bar{\Sigma}(X)$ is real and satisfies the original SD equation on the real axis:

$$\bar{\Sigma}(X) = C_2 \frac{3}{16\pi^2} \left[\int_0^X dY \frac{Y}{X} + \int_X^\infty dY \right] \frac{\bar{g}^2(X+Y)\bar{\Sigma}(Y)}{Y + \bar{\Sigma}(Y)^2}. \tag{3.6}$$

Note that the fermion propagator S_F does not have any poles since the kinetic part x and the mass part $\Sigma^2(x)$ have the same phases as $x + \Sigma^2(x) = e^{i\theta}[X + \bar{\Sigma}^2(X)]$ [see Eq. (3.5)] and the mass function in the space-like region satisfies $X + \bar{\Sigma}^2(X) > 0$.

We should note that the above solution in Eq. (3.5) is a double-valued function on the complex plane: The variable $x = Xe^{i\theta}$ can be parametrized as $x = Xe^{i(\theta + 2\pi)}$ for which the solution takes $\Sigma(x) = e^{i(\theta/2 + \pi)}\bar{\Sigma}(X) = -e^{i\theta/2}\bar{\Sigma}(X)$. This corresponds to the fact that the SD equation has two solutions: When $\Sigma(x)$ is a solution, $-\Sigma(x)$ also satisfies the equation. When we choose the range of θ as $\theta \in [-\pi : \pi]$, the branch cut emerges on the time-like axis. This choice is natural because the appearance of the branch cut in the time-like region seems consistent with the analytic structure of the running coupling. We will see that this branch cut does not matter in calculating the bound state masses.

IV. HOMOGENEOUS BETHE-SALPETER EQUATION

In this section we briefly review the homogeneous Bethe-Salpeter (HBS) equation for the bound states of quark and antiquark and show how to solve it numerically.

A. Bethe-Salpeter amplitude

In this paper, we consider the scalar, pseudoscalar, vector, and axial-vector bound states of quark and antiquark, and we write these bound states as $|S(q)\rangle$, $|P(q)\rangle$, $|V(q,\epsilon)\rangle$, and $|A(q,\epsilon)\rangle$, respectively. Here, q^μ represents the momentum of the bound states and ϵ^μ represents the polarization vector satisfying $\epsilon \cdot q = 0$ and $\epsilon^2 = -1$.

Now, we introduce the Bethe-Salpeter (BS) amplitudes χ for the bound states of quark and antiquark as follows:

$$\langle 0|T\psi_{\alpha f i}(x_+)\bar{\psi}_\beta^{f'j}(x_-)|S_a(q)\rangle = \delta_i^j \frac{(\lambda_a)_f^{f'}}{\sqrt{2}} e^{-iqX} \int \frac{d^4p}{(2\pi)^4} e^{-ipr}[\chi_{(S)}(p;q)]_{\alpha\beta}, \tag{4.1}$$

$$\langle 0|T\psi_{\alpha f i}(x_+)\bar{\psi}_\beta^{f'j}(x_-)|P_a(q)\rangle = \delta_i^j \frac{(\lambda_a)_f^{f'}}{\sqrt{2}} e^{-iqX} \int \frac{d^4p}{(2\pi)^4} e^{-ipr}[\chi_{(P)}(p;q)]_{\alpha\beta}, \tag{4.2}$$

$$\langle 0|T\psi_{\alpha f i}(x_+)\bar{\psi}_\beta^{f'j}(x_-)|V_a(q,\epsilon)\rangle = \delta_i^j \frac{(\lambda_a)_f^{f'}}{\sqrt{2}} e^{-iqX} \int \frac{d^4p}{(2\pi)^4} e^{-ipr}[\chi_{(V)}(p;q,\epsilon)]_{\alpha\beta}, \tag{4.3}$$

$$\langle 0|T\psi_{\alpha f i}(x_+)\bar{\psi}_\beta^{f'j}(x_-)|A_a(q,\epsilon)\rangle = \delta_i^j \frac{(\lambda_a)_f^{f'}}{\sqrt{2}} e^{-iqX} \int \frac{d^4p}{(2\pi)^4} e^{-ipr}[\chi_{(A)}(p;q,\epsilon)]_{\alpha\beta}, \tag{4.4}$$
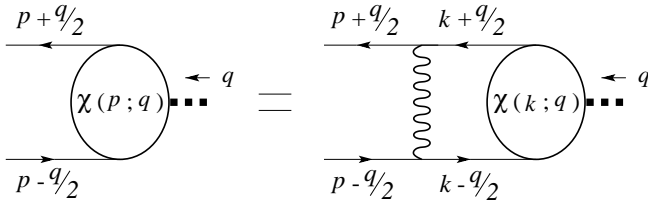
FIG. 9. A graphical representation of the HBS equation in the (improved) ladder approximation.

where $x_\pm = X \pm r/2$, λ_a is the generator of SU(N_f) normalized as tr$[\lambda_a \lambda_b] = 2\delta_{ab}$, and (α, β), (f, f'), and (i, j) denote the spinor, flavor, and color indices, respectively.

We can expand the BS amplitude χ in terms of the bispinor bases Γ^i and the invariant amplitudes χ^i as follows:

$$[\chi_{(S,P)}(p;q)]_{\alpha\beta} = \sum_{i=1}^{4} [\Gamma^i_{(S,P)}(p;q)]_{\alpha\beta} \chi^i_{(S,P)}(p;q),$$
(4.5)

$$[\chi_{(V,A)}(p;q,\epsilon)]_{\alpha\beta} = \sum_{i=1}^{8} [\Gamma^i_{(V,A)}(p;q,\epsilon)]_{\alpha\beta} \chi^i_{(V,A)}(p;q).$$
(4.6)

The bispinor bases can be determined from spin, parity, and charge conjugation properties of the bound states. The explicit forms of $\Gamma^i_{(S)}$, $\Gamma^i_{(P)}$, $\Gamma^i_{(V)}$, and $\Gamma^i_{(A)}$ are summarized in Appendix B.

We take the rest frame of the bound state as a frame of reference:

$$q^\mu = (M_B, 0, 0, 0),$$
(4.7)

where M_B represents the bound state mass. After the Wick rotation, we parametrize p^μ by the real variables u and x as

$$p \cdot q = iM_B u, \quad p^2 = -u^2 - x^2.$$
(4.8)

Consequently, the invariant amplitudes χ^i become functions in u and x:

$$\chi^i_{(S,P,V,A)} = \chi^i_{(S,P,V,A)}(u,x).$$
(4.9)

From the charge conjugation properties for the BS amplitude χ and the bispinor bases defined in Appendix B, the invariant amplitudes $\chi^i(u,x)$ are shown to satisfy the following relation:

$$\chi^i_{(S,P,V,A)}(u,x) = \chi^i_{(S,P,V,A)}(-u,x).$$
(4.10)

B. HBS equation

The HBS equation is the self-consistent equation for the BS amplitude (see, for a review, Ref. [14]), and it is expressed as (see Fig. 9)

$$T\chi = K\chi.$$
(4.11)

The kinetic part T is given by

$$T(p;q) = iS_F^{-1}(p+q/2) \otimes iS_F^{-1}(p-q/2),$$
(4.12)

where S_F is the full fermion propagator $[iS_F^{-1}(p) = \not{p} - \Sigma]$, and the BS kernel K in the improved ladder approximation is expressed as

$$K(p;k) = \frac{N_c^2 - 1}{2N_c} \frac{\bar{g}^2(p,k)}{(p-k)^2} \left(g_{\mu\nu} - \frac{(p-k)_\mu (p-k)_\nu}{(p-k)^2} \right) \cdot \gamma^\mu$$

$$\otimes \gamma^\nu.$$
(4.13)

In the above expressions we used the tensor product notation

$$(A \otimes B)\chi = A\chi B,$$
(4.14)

and the inner product notation

$$K\chi(p;q) = \int \frac{d^4k}{i(2\pi)^4} K(p,k)\chi(k;q).$$
(4.15)

It should be noticed that the fermion propagators included in T in Eq. (4.12) have complex-valued arguments after the Wick rotation. The arguments of the mass functions appearing in two legs of the BS amplitude are expressed as

$$-(p \pm q/2)^2 = u^2 + x^2 - \left(\frac{M_B}{2} \right)^2 \mp iuM_B.$$
(4.16)

In general, it is difficult to obtain mass functions for complex arguments. However, as we have shown in Sec. III, it is easy to obtain them in the case of large N_f QCD.

We now modify Eq. (4.11) so that we can solve it numerically.[4] It is convenient to introduce the conjugate bispinor bases defined by

$$\bar{\Gamma}^i(p;q,\epsilon) \equiv \gamma_0 \Gamma^i(p^*;q,\epsilon)^\dagger \gamma_0.$$
(4.17)

Multiplying these conjugate bispinor bases from the left, taking the trace of spinor indices, and summing over the polarizations, we rewrite Eq. (4.11) into the following form:

$$T_{ij}(u,x)\chi^j(u,x) = \int \frac{y^2 dy dv}{8\pi^3} K_{ij}(u,x;v,y)\chi^j(v,y),$$
(4.18)

where the summation over the index j is understood, and

$$T_{ij}(u,x) = \sum_\epsilon \frac{1}{3} \text{tr}[\bar{\Gamma}^i(p;q,\epsilon)T(p;q)\Gamma^j(p;q,\epsilon)],$$
(4.19)

---

[4]In the following we explain the method for the vector and axial-vector bound states. The extension to the scalar and pseudoscalar bound states is easily done.

$$K_{ij}(u,x;v,y) = \int_{-1}^{1} d\cos\theta \sum_{\epsilon} \frac{1}{3}$$

$$\times \text{tr}[\bar{\Gamma}^i(p;q,\epsilon)K(p,k)\Gamma^j(k;q,\epsilon)],$$

(4.20)

with the real variables v and y introduced as $k \cdot q = iv M_B$ and $k \cdot p = -uv - xy \cos\theta$. Here, we note that although the mass function $\Sigma(x)$ has the branch cut on the time-like axis as mentioned in Sec. III, T_{ij} has no singularity and becomes a continuous function for all the range of u and x. As for K_{ij}, the branch cut of running coupling $\bar{g}$ does not matter since its argument $(p_E^2 + k_E^2)$ never takes a negative value.

Using the property of χ^i in Eq. (4.10), we restrict the integration range as $v > 0$:

$$\int dv K_{ij}(u,x;v,y)\chi^j(v,y)$$

$$= \int_{v>0} dv [K_{ij}(u,x;v,y) + K_{ij}(u,x;-v,y)]\chi^j(v,y).$$

(4.21)

Then, all the variables u, x, v, and y can be treated as positive values.

To discretize the variables u, x, v, and y we introduce new variables U, X, V, and Y as

$$u = \Lambda e^{U/\Lambda}, \quad x = \Lambda e^{X/\Lambda},$$

$$v = \Lambda e^{V/\Lambda}, \quad y = \Lambda e^{Y/\Lambda},$$

(4.22)

and set UV and IR cutoffs as

$$U, V \in [\lambda_U, \Lambda_U], \quad X, Y \in [\lambda_X, \Lambda_X].$$

(4.23)

We discretize the variables U and V into $N_{BS,U}$ points evenly, and X and Y into $N_{BS,X}$ points. Then, the original variables are labeled as

$$u_{[I_U]} = \Lambda \exp[\lambda_U/\Lambda + D_U I_U],$$

$$x_{[I_X]} = \Lambda \exp[\lambda_X/\Lambda + D_X I_X],$$

$$v_{[I_V]} = \Lambda \exp[\lambda_U/\Lambda + D_U I_V],$$

$$y_{[I_Y]} = \Lambda \exp[\lambda_X/\Lambda + D_X I_Y],$$

where $I_U, I_V = 0, 1, 2, \ldots (N_{BS,U} - 1)$ and $I_X, I_Y = 0, 1, 2, \ldots (N_{BS,X} - 1)$. The measures D_U and D_X are defined as

$$D_U = \frac{(\Lambda_U - \lambda_U)/\Lambda}{N_{BS,U} - 1}, \quad D_X = \frac{(\Lambda_X - \lambda_X)/\Lambda}{N_{BS,X} - 1}.$$

(4.24)

As a result, the integration is converted into the summation:

$$\int_{v>0} y^2 dy dv \cdots \Rightarrow D_U D_V \sum_{I_V, I_Y} v y^3 \cdots.$$

(4.25)

In order to avoid integrable singularities in the kernel $K(u,x;v,y)$ at $(u,x) = (v,y)$, we adopt the following four-splitting prescription [28]:

$$K_{ij}(u,x,v,y) \Rightarrow \frac{1}{4}[K_{ij}(u,x,v_+,y_+) + K_{ij}(u,x,v_+,y_-)$$

$$+ K_{ij}(u,x,v_-,y_+) + K_{ij}(u,x,v_-,y_-)],$$

(4.26)

where

$$v_{\pm} = \exp\left[V \pm \frac{D_U}{4}\right], y_{\pm} = \exp\left[Y \pm \frac{D_X}{4}\right].$$

(4.27)

C. Fictitious eigenvalue method

Now that all the variables have become discrete and the original integral equation (4.11) turned into a linear algebraic one, we are able to deal it numerically. However, it is difficult to find the bound state mass M_B and the corresponding BS amplitude χ directly since the HBS equation depends on M_B nonlinearly. A way which enables us to solve the nonlinear eigenvalue problem is the *fictitious eigenvalue method* [14]. In this method we introduce a fictitious eigenvalue λ and interpret the HBS equation (4.11) as a linear eigenvalue equation for a given bound state mass M_B:

$$T\chi = \lambda \cdot K\chi.$$

(4.28)

Consequently, the HBS equation turns into an ordinary eigenvalue problem which we can solve by standard algebraic techniques. By adjusting an input mass M_B such that an eigenvalue λ equals unity, we obtain the bound state mass and the corresponding BS amplitude as a solution of the original HBS equation (4.11). In Appendix A, to show the validity of this method, we calculate the mass of the positronium using this method.

V. NUMERICAL ANALYSIS

In this section we show the results of our numerical analysis.

A. Pseudoscalar bound state

As discussed in Sec. II A, the approximation to the argument of the running coupling in Eq. (2.2) breaks the chiral symmetry explicitly [18]. So, before solving the HBS equation for the massive bound states, we solve that for the pseudoscalar bound state and see how much the chiral symmetry is explicitly broken by this approximation.

The mass of the lowest-lying pseudoscalar bound state should become zero because it appears as a Nambu-Goldstone boson when the chiral symmetry is spontaneously broken. So, we substitute zero for the bound state mass and check whether the fictitious eigenvalue λ becomes unity.

We use the following parameters for the calculations:

$$[\lambda_U, \Lambda_U] = [-18.0, 0], \quad [\lambda_X, \Lambda_X] = [-8.5, 0], \quad (5.1)$$

TABLE I. Fictitious eigenvalues obtained by solving Eq. (4.28) for the pseudoscalar bound state with zero mass used as an input.

α_*	λ	α_*	λ
0.89	1.00121	0.95	1.00262
0.90	1.00205	0.96	1.00267
0.91	1.00230	0.97	1.00273
0.92	1.00241	0.98	1.00279
0.93	1.00249	0.99	1.00284
0.94	1.00255	1.00	1.00290

$$N_{BS,U} = N_{BS,X} = 30. \tag{5.2}$$

We calculate the fictitious eigenvalues for several values of α_* and show them in Table I.

We can see that $\lambda = 1$ is satisfied within 0.3% uncertainty. This implies that our calculations actually reproduce the massless Nambu-Goldstone boson within the numerical error, and that the effect of explicit chiral symmetry breaking caused by the approximation for the running coupling is negligible.

B. Vector, axial-vector, and scalar bound states

In this section we show the results of the numerical calculations for the masses of the vector, axial-vector, and scalar bound states. For the UV and IR cutoffs we adjust the values of them in such a way that the dominant supports of the integrands of the decay constant in Eq. (C4) and the normalization condition in Eq. (C5) lie in the energy region between the UV and IR cutoffs. As an example, we show the integrands of the decay constant and the normalization condition for the vector bound states in Appendix D. From these figures, the dominant supports lie in the lower energy region for smaller value of α_*. Then, we use the following α_*-dependent UV and IR cutoffs for the vector and the axial-vector bound states:

$$[\lambda_U, \Lambda_U] = [-12.0 + 22.0 \times (\alpha_* - 1.0), \ -1.0 + 35.0$$
$$\times (\alpha_* - 1.0)], \tag{5.3}$$

$$[\lambda_X, \Lambda_X] = [-5.0 + 22.0 \times (\alpha_* - 1.0), \ -2.0 + 20.0$$
$$\times (\alpha_* - 1.0)]. \tag{5.4}$$

For the scalar bound state, on the other hand, we use the following fixed UV and IR cutoffs:

$$[\lambda_U, \Lambda_U] = [-18.0, 0], \quad [\lambda_X, \Lambda_X] = [-10.0, 0]. \tag{5.5}$$

Although the integrands of the normalization conditions are shown in Appendix D only for the vector bound states, we have checked that the dominant supports always lie within the energy region between UV and IR cutoffs for all kinds of bound states and for all values of α_*. As for the numbers of the discretization, we use
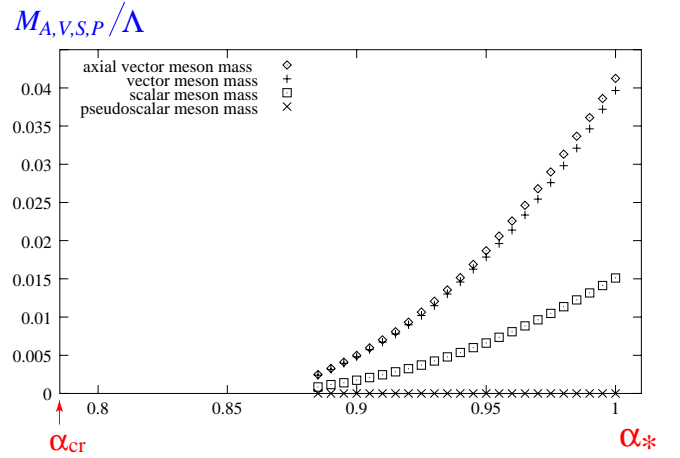

$M_{A,V,S,P}/\Lambda$

FIG. 10. Values of the scalar, pseudoscalar, vector, and axial-vector meson masses for several values of α_*.

$$N_{BS,U} = 20, \quad N_{BS,X} = 55 \tag{5.6}$$

for the vector and the axial-vector bound states, and

$$N_{BS,U} = N_{BS,X} = 30 \tag{5.7}$$

for the scalar bound states. In Appendix D, we show that these numbers of discretization are large enough for the present analysis.

We should stress that we actually found a solution for Eq. (4.28) reproducing $\lambda = 1$ for all the types of the bound states in the range of $\alpha_* \in [0.885:1]$. This means that there do exist the vector, axial-vector, and scalar bound states near the phase transition point in the broken phase.[5]

Now, let us show the critical behavior of the masses of the existing bound states. In Fig. 10, we plot all the bound state masses calculated for several values of α_* together with the pseudoscalar meson masses obtained in the previous section.

This figure shows that the masses of the vector, axial-vector and scalar bound states go to zero simultaneously as the coupling approaches its critical value (or, equivalently, $N_f \to N_f^{\text{crit}}$):

$$M_S, M_V, M_A \to 0 \quad \text{for } \alpha_* \to \alpha_{\text{cr}}. \tag{5.8}$$

Next, to study the critical behavior of M_S, M_V, and M_A we use the function of the form in Eq. (2.19) and fit the value of d by minimizing

$$\sum_{\alpha_*} |M_{S,V,A}(\alpha_*) - h(\alpha_*)|^2. \tag{5.9}$$

The resultant best fitted values of d for the scalar, vector, and axial-vector bound states are

---

[5]On the other hand, we cannot find any solutions for the HBS equations in the symmetric phase, i.e., $\alpha_* < \alpha_{\text{cr}}$ (or, equivalently, $N_f > N_f^{\text{crit}}$). This fact seems consistent with the property of the conformal phase transition which has no bound states in the symmetric phase [3,4].
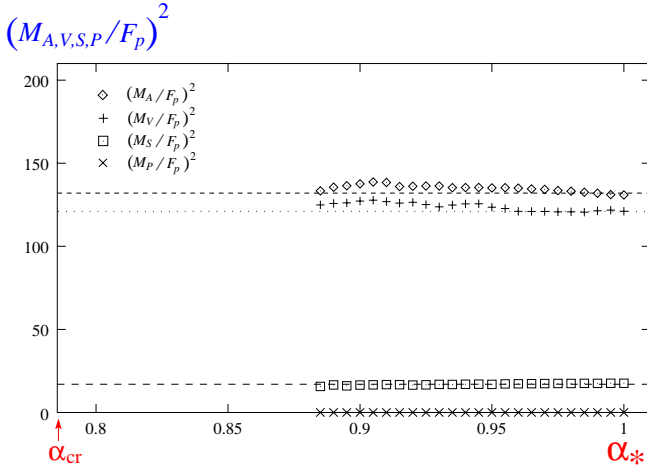
$$\left(M_{A,V,S,P}/F_P\right)^2$$

FIG. 11. Values of $(M_A/F_P)^2$, $(M_V/F_P)^2$, $(M_S/F_P)^2$, and $(M_P/F_P)^2$ for several values of α_* (indicated by $\diamond$, $+$, $\square$, and $\times$, respectively). Dotted lines represent the values of $(M_A/F_P)^2$ $=17$, $(M_V/F_P)^2=121$, and $(M_S/F_P)^2=132$ obtained from Eqs. (5.10) and (2.24).

$$d_{M_S} \simeq 6.2, \quad d_{M_V} \simeq 16.5, \quad d_{M_A} \simeq 17.2, \quad (5.10)$$

respectively. We also plot (the square of) the ratio of the bound state masses to F_P for several values of α_* in Fig. 11.

The dotted lines plotted together with the data in this figure represent the values of the following ratios obtained from Eqs. (5.10) and (2.24):

$$(M_S/F_P)^2=17, \quad (M_V/F_P)^2=121, \quad (M_A/F_P)^2=132. \quad (5.11)$$

This figure clearly shows that all the masses of the scalar, vector, and axial-vector bound states have the same scaling property as that of F_P:

$$\frac{M_{S,V,A}}{F_P} \sim \text{ constant.} \quad (5.12)$$

We can also say that these masses have the same scaling property as that of $\Sigma(m^2)$ since F_P and $\Sigma(m^2)$ have the same scaling property. Their ratios are summarized as follows:

$$\Sigma^2(m^2):M_S^2:M_V^2:M_A^2=1:2.4:17.0:18.5. \quad (5.13)$$

One might think that the vector and axial-vector bound states decay into a fermion and an antifermion since $M_V^2 > 4\Sigma^2(m^2)$ and $M_A^2 > 4\Sigma^2(m^2)$. However, this does not happen: As we noticed above Eq. (2.18), $\Sigma(m^2)$ is not the pole mass but the dynamical mass defined in the space-like region. Furthermore, as we have shown in Sec. III, the fermion propagators do not have any poles in the entire complex plane including the time-like axis where the pole mass of fermion should be defined. Thus the vector and axial-vector bound states do not decay into a fermion and an antifermion.

VI. CONCLUSION AND DISCUSSION

In this paper we first pointed out that, when we solve the Schwinger-Dyson (SD) equation in large N_f QCD, we do not need to introduce any IR regularizations for the running coupling since it takes a finite value for all the range of the energy region due to the existence of the IR fixed point. In the case of small N_f, we have to regularize the IR divergence of the running coupling, and different schemes of regularizations would give different results. Furthermore, it is difficult to find the regularization which makes the analytic structure of the running coupling simple enough. On the contrary, the solution of the two-loop RGE in large N_f QCD is explicitly written in terms of the Lambert W function, and the running coupling does not have any singularities on the complex plane except for the time-like axis when N_f is close to N_f^{crit}. This significant feature of the running coupling in large N_f QCD enabled us to solve the SD equation on the complex plane.

Then, we solved the homogeneous Bethe-Salpeter (HBS) equations for the scalar, pseudoscalar, vector, and axial-vector bound states of quark and anti-quark in large N_f QCD with the improved ladder approximation in the Landau gauge. In the quark propagator included in the HBS equation, we used the quark mass function obtained from the SD equation with the same approximation, which is needed for the consistency with the chiral symmetry.

We first showed that the HBS equation provides the massless pseudoscalar bound state in the broken phase which is identified with the Nambu-Goldstone boson associated with the spontaneous breaking of the chiral symmetry. Next, we showed that there actually exist vector, axial-vector, and scalar bound states even near the phase transition point in the broken phase, and that their masses decreases as the number of massless quarks N_f increases. At the critical point all the masses go to zero, showing the same scaling property as that of the pseudoscalar meson decay constant F_P consistently with the picture expected from the conformal phase transition [3,13].

Let us discuss the pattern of the chiral symmetry restoration by considering the representation of chiral $SU(N_f)_L \times SU(N_f)_R$ of the low-lying mesons extending the analyses done in Refs. [39,40].

For $N_f=3$ the pseudoscalar meson denoted by π and the longitudinal axial-vector meson denoted by A_1 are an admixture of $(8,1) \oplus (1,8)$ and $(3,3^*) \oplus (3^*,3)$, since the chiral symmetry is spontaneously broken [39,40]

$$|\pi\rangle = |(3,3^*) \oplus (3^*,3)\rangle \sin\psi + |(8,1) \oplus (1,8)\rangle \cos\psi,$$

$$|A_1(\lambda=0)\rangle = |(3,3^*) \oplus (3^*,3)\rangle \cos\psi$$
$$- |(8,1) \oplus (1,8)\rangle \sin\psi, \quad (6.1)$$

where λ denotes the helicity in the collinear frame, and the experimental value of the mixing angle ψ is given by approximately $\psi = \pi/4$ [40]. On the other hand, the longitudinal vector meson denoted by ρ belongs to pure $(8,1) \oplus (1,8)$ and the scalar meson denoted by S to pure $(3,3^*) \oplus (3^*,3)$:

$$|\rho(\lambda=0)\rangle=|(8,1)\oplus(1,8)\rangle,$$

$$|S\rangle=|(3,3^*)\oplus(3^*,3)\rangle. \qquad (6.2)$$

When the chiral symmetry is restored at the phase transition point, it is natural that the chiral representations coincide with the mass eigenstates: The representation mixing is dissolved. From Eq. (6.1) one can easily see that there are two ways to express the representations in the Wigner phase of the chiral symmetry: The conventional manifestation *á la* the linear sigma model (called the GL manifestation in Ref. [11]) corresponds to the limit $\psi\to\pi/2$ in which $|\pi\rangle$ is in the representation of pure $(N_f,N_f^*)\oplus(N_f^*,N_f)$ of SU$(N_f)_{\rm L}$ $\times$SU$(N_f)_{\rm R}$ together with the scalar meson, both being the chiral partners:

$$\text{(GL)} \quad \begin{cases} |\pi\rangle,|S\rangle\to|(N_f,N_f^*)\oplus(N_f^*,N_f)\rangle, \\ |A_1(\lambda=0)\rangle,|\rho(\lambda=0)\rangle\to|(N_f^2-1,1)\oplus(1,N_f^2-1)\rangle. \end{cases} \qquad (6.3)$$

On the other hand, the vector manifestation (VM) [10] corresponds to the limit $\psi\to0$ in which the A_1 goes to a pure $(N_f,N_f^*)\oplus(N_f^*,N_f)$, now degenerate with the scalar meson in the same representation, but not with ρ in $(N_f^2-1,1)\oplus(1,N_f^2-1)$:

$$\text{(VM)} \quad \begin{cases} |\pi\rangle,|\rho(\lambda=0)\rangle\to|(N_f^2-1,1)\oplus(1,N_f^2-1)\rangle, \\ |A_1(\lambda=0)\rangle,|S\rangle\to|(N_f,N_f^*)\oplus(N_f^*,N_f)\rangle. \end{cases} \qquad (6.4)$$

Namely, the degenerate massless π and (longitudinal) ρ at the phase transition point are the chiral partners in the representation of $(N_f^2-1,1)\oplus(1,N_f^2-1)$.

Now, what does our result say on the chiral representation of low-lying mesons? As can be seen from Fig. 11, the resultant values of the masses obtained from the HBS equation roughly satisfies the following relation [40]:

$$M_A^2+M_P^2=M_V^2+M_S^2, \qquad (6.5)$$

for all values of α_*. This relation holds independently of the mixing angle ψ given in Eq. (6.1) when the low-lying mesons saturate the chiral algebra shown in Ref. [40]. Then, it is reasonable to discuss the chiral representation without worrying about the influence of the excited states of the bound states. By using the relation $\tan\psi=M_V/M_S$ [40] and the values of M_V and M_S obtained from the HBS equation in Sec. V B, the value of the mixing angle ψ is roughly determined as

$$\tan\psi=M_V/M_S\sim3. \qquad (6.6)$$

This implies that π and the longitudinal A_1 are still admixtures of the pure chiral representation even at the chiral restoration point:

$$|\pi\rangle\to|(N_f,N_f^*)\oplus(N_f^*,N_f)\rangle\sin\psi$$
$$+|(N_f^2-1,1)\oplus(1,N_f^2-1)\rangle\cos\psi,$$

$$|A_1\rangle\to|(N_f,N_f^*)\oplus(N_f^*,N_f)\rangle\cos\psi$$
$$-|(N_f^2-1,1)\oplus(1,N_f^2-1)\rangle\sin\psi. \qquad (6.7)$$

This may suggest the existence of a new type of manifestation of chiral symmetry restoration in large N_f QCD which is neither of the GL manifestation nor the simple version of the vector manifestation (VM).

Several comments are in order.

In Appendix C, we show the calculations of the coupling constants F_V, F_A, and G_S of the vector, axial-vector, and scalar bound states to the vector current, axial-vector current, and scalar density. The results shows that they also have the same scaling properties as F_P. These results indicate that all the dimension-full quantities determined by the IR dynamics have the same scaling properties, as far as the (improved) ladder approximation is concerned.

Although the masses obtained from the HBS equation satisfy the condition (6.5) needed for the saturation of the chiral algebra, the couplings F_P, F_V, and F_A do not seem to satisfy the first Weinberg's sum rule [41]: $F_P^2+F_A^2=F_V^2$. We have not fully understood what this means for the pattern of chiral symmetry restoration. Apparently, reducing the numerical uncertainty will help us to reach the final understanding.

In the present analysis we did not include the effect from the four-fermion interaction which is induced in the case of $\gamma_m\simeq1$ as was conjectured in strong coupling QED [32] and was demonstrated in walking gauge theories [42,43]. It is not clear at this moment whether or not the qualitative results in the present analysis will be changed when we include such an effect.

In the present analysis we stressed that the running coupling in large N_f QCD determined from a two-loop β function is expressed as the Lambert W function which enables us to solve the HBS and SD equations with mutual consistency near the critical point. Apparently, this Lambert W function can be used as an IR regularization to solve the HBS and SD equations with mutual consistency in the case

of QCD with small N_f. It will be very interesting to study meson masses near the chiral phase transition in hot and/or dense QCD by using such an IR regularization.

We think that it is important to clarify which effective field theory (EFT) describes the new pattern of the chiral symmetry restoration expressed in Eq. (6.7). Especially, it is very interesting to see how the matching between the EFT and the underlying QCD with large N_f can be done to determine bare parameters of the Lagrangian of the EFT.

ACKNOWLEDGMENTS

APPENDIX A: POSITRONIUM

In this appendix, to show the validity of the fictitious eigenvalue method for solving the HBS equation explained in Sec. IV C, we calculate the mass of the orthopositronium which is the vector bound state of the electron and the positron. The same analysis was done in Ref. [38], and here we follow the analysis.

In the weak coupling limit the HBS equation for the orthopositronium can be solved analytically, and the energy spectrum takes the following form [44]:

$$M_V^{(n)} = 2m_e - \frac{m_e \alpha^2}{4n^2}, \qquad \text{(A1)}$$

where m_e is the mass of the electron and the positron, and $\alpha = 1/137$ is the coupling constant of QED.

We use following parameters in our calculation:

$$[\lambda_U, \Lambda_U] = [-18.5, -2.9], [\lambda_X, \Lambda_X] = [-10.8, 2.2], \qquad \text{(A2)}$$

$$N_{BS,U} = N_{BS,X} = 28, \quad m_e = 137.0. \qquad \text{(A3)}$$

(We used the energy scale which satisfies the relation $m_e \alpha = 1$ following Ref. [38].) In Fig. 12, we show the resultant values of the fictitious eigenvalue λ for several values of the input parameter M_V.

Finding the point where the smallest λ becomes unity, we determine the value of the mass of the ground state $M_V^{(1)}$ as the solution of the original HBS equation:

$$M_V^{(1)} = 273.99842. \qquad \text{(A4)}$$

From this the binding energy is calculated as

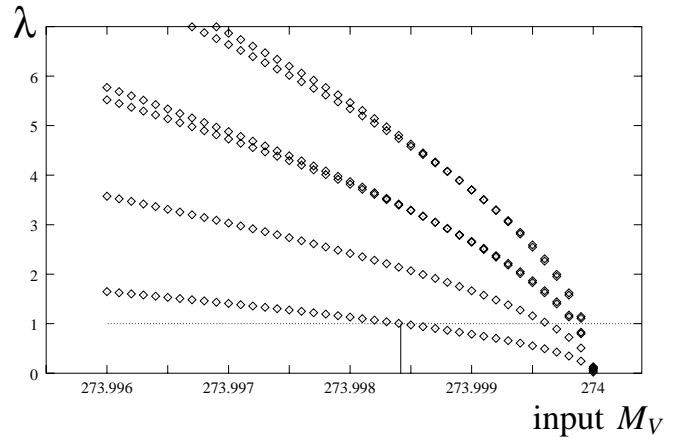$$E^{(1)} = 0.00158. \qquad \text{(A5)}$$

FIG. 12. Fictitious eigenvalues for the positronium.

These values are in good agreement with the values $M_V^{(1)} = 273.99817$ and $E^{(1)} = 0.00183$ derived from Eq. (A1). This shows that our numerical method works well to obtain the mass of the ground state.

APPENDIX B: BISPINOR BASES FOR SCALAR, PSEUDOSCALAR, VECTOR, AND AXIAL-VECTOR BOUND STATES

In this appendix we show the explicit forms of the bispinor bases for the scalar, pseudoscalar, vector, and axial-vector bound states. Here, we use the notation $\hat{q}_\mu = q_\mu / M_B$ with M_B being the mass of the bound states, and $[a,b,c] \equiv a[b,c] + b[c,a] + c[a,b]$.

The bispinor base for the scalar bound state ($J^{PC} = 0^{++}$) is given by

$$\Gamma^1_{(S)} = \mathbf{1}, \quad \Gamma^2_{(S)} = \not{p}, \quad \Gamma^3_{(S)} = \hat{\not{q}}(p \cdot \hat{q}), \quad \Gamma^4_{(S)} = \frac{1}{2}[\not{p}, \hat{\not{q}}], \qquad \text{(B1)}$$
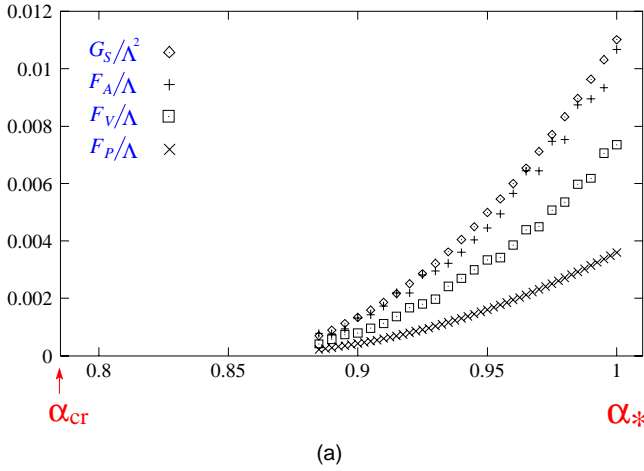
and that for the pseudoscalar bound state ($J^{PC} = 0^{-+}$) is given by

$$\Gamma^1_{(P)} = \gamma_5, \quad \Gamma^2_{(P)} = \not{p}(p \cdot \hat{q})\gamma_5,$$

$$\Gamma^3_{(P)} = \hat{\not{q}}\gamma_5, \quad \Gamma^4_{(P)} = \frac{1}{2}[\not{p}, \hat{\not{q}}]\gamma_5. \qquad \text{(B2)}$$
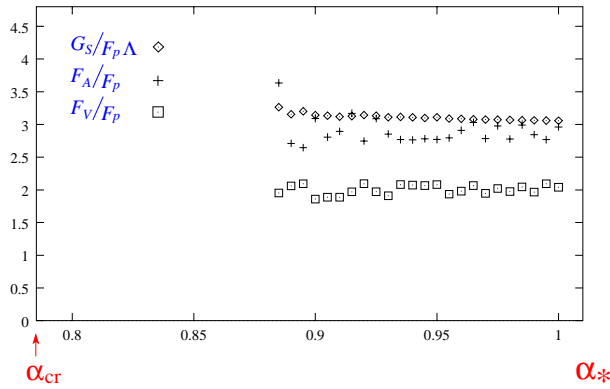
Furthermore, for the vector bound state ($J^{PC} = 1^{--}$) we use

$$\Gamma^1_{(V)} = \not{\epsilon}, \quad \Gamma^2_{(V)} = \frac{1}{2}[\not{\epsilon}, \not{p}](p \cdot \hat{q}),$$

$$\Gamma^3_{(V)} = \frac{1}{2}[\not{\epsilon}, \hat{\not{q}}], \quad \Gamma^4_{(V)} = \frac{1}{3!}[\not{\epsilon}, \not{p}, \hat{\not{q}}],$$

$$\Gamma^5_{(V)} = (\epsilon \cdot p), \quad \Gamma^6_{(V)} = \not{p}(\epsilon \cdot p),$$

$$\Gamma^7_{(V)} = \hat{\not{q}}(p \cdot \hat{q})(\epsilon \cdot p), \quad \Gamma^8_{(V)} = \frac{1}{2}[\not{p}, \hat{\not{q}}](\epsilon \cdot p),$$

(B3)

G_S/Λ^2, $F_{A,V,P}/\Lambda$

(a)

$G_S/F_P\Lambda$, $F_{A,V}/F_P$

(b)

FIG. 13. Values of (a) F_V, F_A, G_S, and F_P and (b) G_S/F_P, F_V/F_P, and F_A/F_P for several values of α_*.

and for the axial-vector bound state ($J^{PC}=1^{++}$)

$$\Gamma_{(A)}^1 = \not{k}\gamma_5, \quad \Gamma_{(A)}^2 = \frac{1}{2}[\not{k},\not{p}]\gamma_5, \quad \Gamma_{(A)}^3 = \frac{1}{2}[\not{k},\hat{\not{q}}](p\cdot\hat{q})\gamma_5,$$

$$\Gamma_{(A)}^4 = \frac{1}{3!}[\not{k},\not{p},\hat{\not{q}}]\gamma_5, \quad \Gamma_{(A)}^5 = (\epsilon\cdot p)(p\cdot\hat{q})\gamma_5,$$

$$\Gamma_{(A)}^6 = \not{p}(\epsilon\cdot p)\gamma_5, \quad \Gamma_{(A)}^7 = \hat{\not{q}}(\epsilon\cdot p)(p\cdot\hat{q})\gamma_5,$$

$$\Gamma_{(A)}^8 = \frac{1}{2}[\not{p},\hat{\not{q}}](\epsilon\cdot p)(p\cdot\hat{q})\gamma_5. \tag{B4}$$

APPENDIX C: COUPLING CONSTANTS TO CURRENTS AND SCALAR DENSITY

In this section we calculate coupling constants F_V, F_A, and G_S of the vector, axial-vector, and scalar bound states to the vector current, axial-vector current, and scalar density. They are defined by
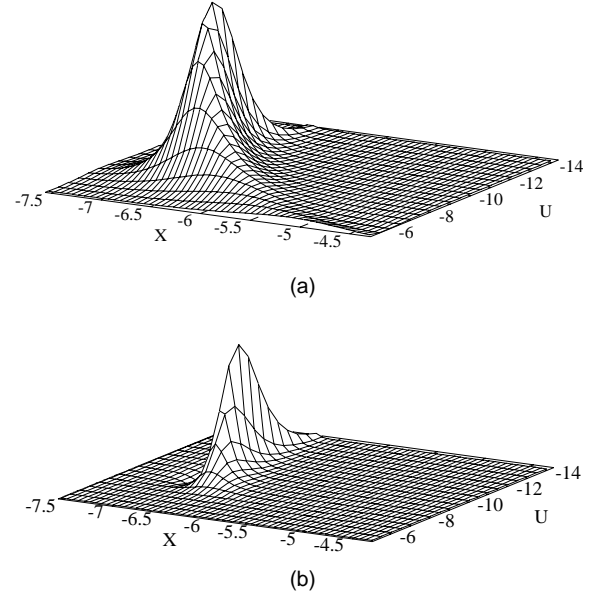

(a)

(b)

FIG. 14. Integrands of (a) the decay constant in Eq. (C4) and (b) the normalization condition in Eq. (C5) for $\alpha_* = 0.885$.

$$\langle 0|\bar{\psi}(0)\gamma^\mu\frac{\lambda_a}{2}\psi(0)|V_b(q,\epsilon)\rangle = \delta_{ab}F_V M_V\epsilon^\mu, \tag{C1}$$

$$\langle 0|\bar{\psi}(0)\gamma^\mu\gamma_5\frac{\lambda_a}{2}\psi(0)|A_b(q,\epsilon)\rangle = \delta_{ab}F_A M_A\epsilon^\mu, \tag{C2}$$

$$\langle 0|\bar{\psi}(0)\frac{\lambda_a}{2}\psi(0)|S_b(q,\epsilon)\rangle = \delta_{ab}G_S, \tag{C3}$$

where λ_a is the flavor matrix normalized as $\text{tr}[\lambda_a\lambda_b] = 2\delta_{ab}$.

By using the BS amplitudes for the vector bound state, F_V is expressed as

$$F_V M_V = -\frac{\sqrt{2}iN_c}{\pi^3}\int_0^\infty du\int_0^\infty dx\left[x^2\chi^1(u,x) - \frac{x^4}{3}\chi^6(u,x)\right]. \tag{C4}$$

In the above expression, the normalization of the BS amplitudes χ^i are determined by the following normalization condition [14]:

$$2M_V\delta_{\epsilon\epsilon'} = iN_c\int\frac{d^4p}{(2\pi)^4}\left[\bar{\chi}(p;q,\epsilon)\frac{\partial T(p;q)}{\partial M_V}\chi(p;q,\epsilon')\right]. \tag{C5}$$

Here, we notice again that $T(p;q)$ has no singularity although the fermion propagator S_F has a branch cut in the time-like region. So the integral in Eq. (C5) is well-defined. Once we have obtained M_V and the corresponding BS amplitudes by solving the HBS equation, we can calculate F_V from Eq. (C4). We can also calculate F_A and G_S in a similar way. In Fig. 13(a) we show the values of F_V, F_A, and G_S together with F_P for several values of α_*.
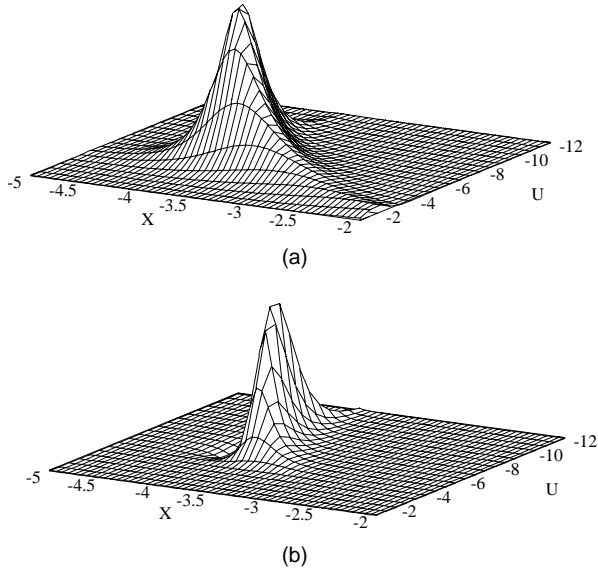
(a)

(b)

FIG. 15. Integrands of (a) the decay constant in Eq. (C4) and (b) the normalization condition in Eq. (C5) for $\alpha_* = 1.0$.

To see the scaling properties, we plot the ratio of F_V, F_A, and G_S to F_P in Fig. 13(b). This figure shows that F_V, F_A, and G_S have the same scaling properties as that of F_P.

APPENDIX D: UNCERTAINTIES FOR NUMERICAL CALCULATIONS

To solve the HBS equation for the bound states numerically, we introduced the UV and IR cutoffs and converted the HBS equation into a linear eigenvalue equation by discretizing the integral. As we have discussed in Sec. V B, we adjust the values of the UV and IR cutoffs in such a way that the dominant supports of the integrands of the decay constant in Eq. (C4) and the normalization condition in Eq. (C5) lie in the energy region between the UV and IR cutoffs. In Figs. 14 and 15 we show those integrands for $\alpha_* = 0.885$ and 1.0 in the case of the vector bound state.

These figures show that the dominant supports lie in the lower energy region for a smaller value of α_*, and that the present choices in Eqs. (5.3) and (5.4) cover the supports. For other values of α_* used in the present analysis we have checked that the dominant supports always lie within the energy region between the UV and IR cutoffs chosen as in Eqs. (5.3) and (5.4).

As for the numbers of the discretization, due to the limitation of the computer resources we used $N_{BS,U} = 20$ and $N_{BS,X} = 55$ as shown in Eq. (5.6). Here we study the dependences of the mass and the decay constant of the vector bound state on the size of discretization. We show the typical
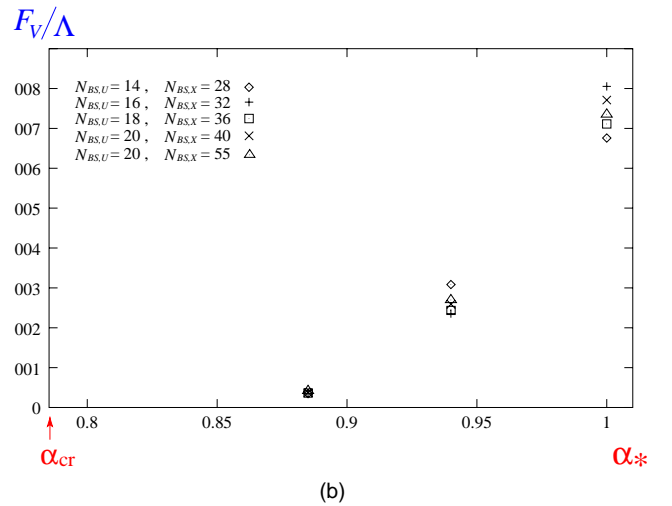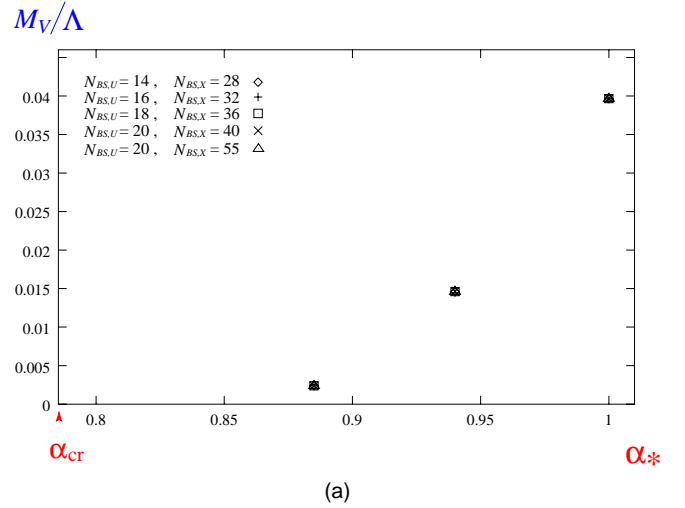

(a)

(b)

FIG. 16. Typical values of (a) M_V/Λ and (b) F_V/Λ for five choices of the size of discretization, $(N_{BS,U},N_{BS,X})=(14,28)$, (16,32), (18,36), (20,40), and (20,55).

values of the mass in Fig. 16(a) and those of the decay constant in Fig. 16(b) for five choices of the size of the discretization, $(N_{BS,U},N_{BS,X})=(14,28)$, (16,32), (18,36), (20,40), and (20,55).

Figure 16(a) clearly shows that the choice $(N_{BS,U},N_{BS,X})=(20,55)$ is large enough to obtain the mass of the vector bound state. On the other hand, Fig. 16(b) shows that there are still uncertainties in the value of the decay constant which come from the size of the discretization. Apparently, this uncertainty from the size of discretization is the dominant part of the numerical uncertainties in the present analysis.

[1] T. Banks and A. Zaks, Nucl. Phys. **B196**, 189 (1982).
[2] T. Appelquist, J. Terning, and L.C. Wijewardhana, Phys. Rev. Lett. **77**, 1214 (1996).
[3] V.A. Miransky and K. Yamawaki, Phys. Rev. D **55**, 5051 (1997); **56**, 3768(E) (1997).
[4] T. Appelquist, A. Ratnaweera, J. Terning, and L.C. Wijewardhana, Phys. Rev. D **58**, 105017 (1998).
[5] J.B. Kogut and D.K. Sinclair, Nucl. Phys. **B295**, 465 (1988);

F.R. Brown, H. Chen, N.H. Christ, Z. Dong, R.D. Mawhinney, W. Schaffer, and A. Vaccarino, Phys. Rev. D **46**, 5655 (1992); Y. Iwasaki, K. Kanaya, S. Sakai, and T. Yoshie, Phys. Rev. Lett. **69**, 21 (1992); Y. Iwasaki, K. Kanaya, S. Kaya, S. Sakai, and T. Yoshie, Nucl. Phys. B (Proc. Suppl.) **53**, 449 (1997); Prog. Theor. Phys. Suppl. **131**, 415 (1998).

[6] R. Oehme and W. Zimmermann, Phys. Rev. D **21**, 471 (1980).

[7] M. Velkovsky and E. Shuryak, Phys. Lett. B **437**, 398 (1998).

[8] T. Hatsuda and T. Kunihiro, Phys. Rep. **247**, 221 (1994); R.D. Pisarski, hep-ph/9503330; G.E. Brown and M. Rho, Phys. Rep. **269**, 333 (1996); F. Wilczek, hep-ph/0003183; G.E. Brown and M. Rho, Phys. Rep. **363**, 85 (2002).

[9] M. Harada and K. Yamawaki, Phys. Rev. Lett. **83**, 3374 (1999).

[10] M. Harada and K. Yamawaki, Phys. Rev. Lett. **86**, 757 (2001).

[11] M. Harada and K. Yamawaki, Phys. Rep. **381**, 1 (2003).

[12] M. Bando, T. Kugo, S. Uehara, K. Yamawaki, and T. Yanagida, Phys. Rev. Lett. **54**, 1215 (1985); M. Bando, T. Kugo, and K. Yamawaki, Phys. Rep. **164**, 217 (1988).

[13] R.S. Chivukula, Phys. Rev. D **55**, 5238 (1997).

[14] N. Nakanishi, Prog. Theor. Phys. Suppl. **43**, 1 (1969).

[15] T. Kugo, in *Proceedings of 1991 Nagoya Spring School on Dynamical Symmetry Breaking*, Nakatsugawa, Japan, 1991, edited by K. Yamawaki (World Scientific, Singapore, 1992).

[16] V.A. Miransky, *Dynamical Symmetry Breaking in Quantum Field Theories* (World Scientific, Singapore, 1993).

[17] T. Maskawa and H. Nakajima, Prog. Theor. Phys. **52**, 1326 (1974); **54**, 860 (1975); M. Bando, M. Harada, and T. Kugo, *ibid.* **91**, 927 (1994).

[18] T. Kugo and M.G. Mitchard, Phys. Lett. B **282**, 162 (1992).

[19] T. Kugo and M.G. Mitchard, Phys. Lett. B **286**, 355 (1992).

[20] M. Bando, M. Harada, and T. Kugo, Prog. Theor. Phys. **91**, 927 (1994).

[21] K. Higashijima, Phys. Rev. D **29**, 1228 (1984).

[22] V.A. Miransky, Sov. J. Nucl. Phys. **38**, 280 (1983) [Yad. Fiz. **38**, 468 (1983)].

[23] K.I. Aoki, M. Bando, T. Kugo, M.G. Mitchard, and H. Nakatani, Prog. Theor. Phys. **84**, 683 (1990).

[24] K.I. Aoki, M. Bando, T. Kugo, and M.G. Mitchard, Prog. Theor. Phys. **85**, 355 (1991).

[25] C.D. Roberts and S.M. Schmidt, Prog. Part. Nucl. Phys. **45**, S1 (2000).

[26] T. Kugo, M.G. Mitchard, and Y. Yoshida, Prog. Theor. Phys. **91**, 521 (1994).

[27] P. Maris, C.D. Roberts, and P.C. Tandy, Phys. Lett. B **420**, 267 (1998).

[28] K.I. Aoki, T. Kugo, and M.G. Mitchard, Phys. Lett. B **266**, 467 (1991).

[29] K. Naito, K. Yoshida, Y. Nemoto, M. Oka, and M. Takizawa, Phys. Rev. C **59**, 1095 (1999); K. Naito and M. Oka, *ibid.* **59**, 542 (1999).

[30] R. Alkofer, P. Watson, and H. Weigel, Phys. Rev. D **65**, 094026 (2002).

[31] E. Gardi and M. Karliner, Nucl. Phys. **B529**, 383 (1998); E. Gardi, G. Grunberg, and M. Karliner, J. High Energy Phys. **07**, 007 (1998).

[32] C.N. Leung, S.T. Love, and W.A. Bardeen, Nucl. Phys. **B273**, 649 (1986); **B323**, 493 (1989).

[33] T. Appelquist, K.D. Lane, and U. Mahanta, Phys. Rev. Lett. **61**, 1553 (1988); H. Georgi, E.H. Simmons, and A.G. Cohen, Phys. Lett. B **236**, 183 (1990).

[34] R.M. Corless, G.H. Gonnet, D.G.E. Hare, D.J. Jeffrey, and D.E. Knuth, Adv. Comput. Math. **5**, 329 (1996).

[35] H. Pagels and S. Stokar, Phys. Rev. D **20**, 2947 (1979).

[36] B. Holdom, Phys. Lett. **150B**, 301 (1985); K. Yamawaki, M. Bando, and K. Matumoto, Phys. Rev. Lett. **56**, 1335 (1986); T. Akiba and T. Yanagida, Phys. Lett. **169B**, 432 (1986); T.W. Appelquist, D. Karabali, and L.C.R. Wijewardhana, Phys. Rev. Lett. **57**, 957 (1986).

[37] T. Kugo and Y. Yoshida, Soryushiron Kenkyu **91**, B26 (1995); Y. Yoshida, Ph.D. thesis, Kyoto University, 1995.

[38] M. Harada and Y. Yoshida, Phys. Rev. D **53**, 1482 (1996).

[39] F.J. Gilman and H. Harari, Phys. Rev. **165**, 1803 (1968).

[40] S. Weinberg, Phys. Rev. **177**, 2604 (1969).

[41] S. Weinberg, Phys. Rev. Lett. **18**, 507 (1967).

[42] K.-I. Kondo, S. Shuto, and K. Yamawaki, Mod. Phys. Lett. A **6**, 3385 (1991).

[43] K.I. Aoki, K. Morikawa, J.I. Sumi, H. Terao, and M. Tomoyose, Prog. Theor. Phys. **102**, 1151 (1999).

[44] See, for example, C. Itzykson and J.B. Zuber, *Quantum Field Theory* (McGraw-Hill, New York, 1980).